Dalton Transactions

ROYAL SOCIETY OF CHEMISTRY

PAPER

View Article Online
View Journal | View Issue

Cite this: *Dalton Trans.*, 2025, **54**, 17471

Hemiparetic koneramine NNP ligand comprising strategic hard and soft donors: transition metal complexes, CS_2 activation and therapeutic potential

Archana Yadav, [a] Sayari Dewan,[a] Kajal Chaudhary,[a] Ray J. Butcher, [b] Ritika Gautam Singh [a] and Raja Angamuthu *[a]

A novel koneramine-derived tridentate NNP ligand has been designed and synthesized, and its coordination chemistry explored with hard and soft metal centres, including Zn(II), Pd(II), Ru(II), Cu(I), Cu(II), and Ni(II). The resulting complexes were characterized by spectroscopic, structural, and electrochemical methods, revealing the ligand's electronic flexibility and its ability to stabilize copper in multiple oxidation states (Cu(I)/Cu(II)) *via* selective donor interactions and adaptable coordination geometries. A ruthenium hydride complex, [Ru(NNP)(H)Cl(CO)], exhibits efficient hydride transfer reactivity and undergoes double carbon disulfide (CS_2) insertion into the Ru–H bond to afford [Ru(NNP)$(CS_2H)_2$(CO)], highlighting its potential in small-molecule activation. Preliminary biological studies show that *syn*- and *anti-rac*-[Ru(NNP)(H)Cl(CO)] display potent antibacterial activity against *S. aureus* ATCC29213 (MIC = 2 μg mL^{-1}), while *anti-rac*-[Ru(NNP)(H)Cl(CO)] and [Zn(NNP)Cl_2] exhibit enhanced anticancer efficacy and lower cytotoxicity toward non-cancerous cells compared to cisplatin, highlighting their therapeutic potential.

Received 2nd September 2025,
Accepted 7th November 2025

DOI: 10.1039/d5dt02106e

rsc.li/dalton

Introduction

The design and development of multifunctional metal complexes exhibiting both catalytic and biological activity represents a rapidly expanding field in organometallic chemistry.[1–5] Multidentate ligands, which provide structural flexibility and electronic tunability, are at the forefront of coordination and organometallic chemistry.[6] Their ability to chelate metal centres through multiple donor atoms enhances thermodynamic stability and governs their kinetic profile during catalytic processes. Koneramines are a new class of tridentate ligands that consist of two pyridyl nitrogens (N1 and N3), one tertiary amine nitrogen (N2), a secondary tertiary nitrogen (N4) and two stereogenic centres. Koneramine ligands have attracted significant attention due to their tridentate coordination mode, ease of modification, and ability to stabilise a wide range of metal centres.[7–12] However, conventional koneramine often shows selectivity toward either hard or soft metals, limiting their versatility. The incorporation of mixed donor atoms (*e.g.*, N, P, S, O) within a ligand scaffold provides electronic flexibility, enabling the stabilization of metal centres in diverse oxidation states, which is particularly important in redox-active systems and catalysis.[13–22]

Carbon disulfide (CS_2) is a colourless volatile liquid used in industries for manufacturing viscose rayon, cellophane, and rubber-processing chemicals.[23] Despite its widespread application, CS_2 is highly toxic and leads to acute or chronic poisoning.[24,25] Relative to its carbon dioxide (CO_2) analogue, CS_2 remains underexplored, largely due to its thermodynamic stability and limited reactivity. Nonetheless, it is a valuable synthon for sulfur-containing heterocycles and other organosulfur compounds with applications in pharmaceuticals and materials science.[26,27] Transition metal hydride complexes exhibit significant potential in promoting the insertion of CO_2 and CS_2 through metal hydride or metal ligand cooperative pathways.[28–40] Despite progress in CO_2 activation using transition metal hydride complexes, analogous studies with CS_2 remain limited.

Alongside catalytic applications, the development of metal complexes as therapeutic agents has emerged as a promising strategy for tackling global health challenges. The escalating threat of multidrug-resistant (MDR) infections and the ongoing global burden of cancer are the two major challenges in contemporary medicine.[41,42] Metal complexes offer unique advantages over traditional organic drugs, including tunable redox activity, ligand exchange dynamics, and the capacity to generate reactive oxygen species.[43–54] Thus, ligand frameworks

[a]*Department of Chemistry, Indian Institute of Technology Kanpur, Kanpur, India, 208016. E-mail: raja@iitk.ac.in*
[b]*Department of Chemistry, Howard University, Washington, D.C, 20059, USA*

that combine catalytic utility with biological relevance are highly desirable.

Copper-containing enzymes such as galactose oxidase, tyrosinase, and multicopper oxidases exploit mixed donor environments to achieve precise control over redox activity, balancing Cu(I) and Cu(II) states through selective interactions with nitrogen, oxygen, and sulfur donors.[55] Inspired by nature, synthetic ligand frameworks combining both hard and soft donor atoms have been developed to stabilize metals across multiple oxidation states, yet achieving predictable control over donor preference remains challenging. In particular, the role of phosphorus donors in tuning Cu(I)/Cu(II) coordination remains underexplored compared to classical N, O, S-based systems.[56]

In this work, we report the design and synthesis of a novel koneramine-based NNP ligand that incorporates both hard (N) and soft (P) donor sites, along with its metal complexes. The dual-donor framework facilitates the stabilization of a wide range of metal centres such as Zn(II), Pd(II), Ru(II), Cu(I), Cu(II), and Ni(II), providing a tunable electronic environment crucial for catalysis and biological applications. The reactivity of the ruthenium hydride complexes toward CS_2 activation was studied to explore their potential in organosulfur synthesis, while *in vitro* anticancer and antibacterial assays were conducted to evaluate the therapeutic potential of the ligand and its metal complexes.

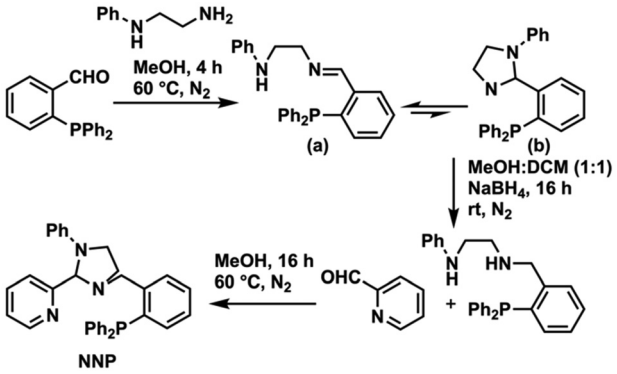

Scheme 1 Synthesis of NNP ligand.

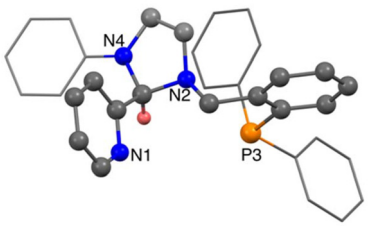

Fig. 1 Solid-state structure of NNP ligand. H atoms other than those bound to the stereogenic centre are omitted for clarity. Interatomic distances and angles are provided in the SI (Fig. S93 and Table S1).

Results and discussion

Conventional koneramines often exhibit selective binding toward either hard or soft metal centres, depending on the nature and electronic characteristics of the nitrogen donor atoms within the ligand framework. This selectivity arises from the HSAB (Hard and Soft Acids and Bases) principle, where the spatial arrangement and electronic tuning of donor groups influence the ligand's affinity for specific metals. To enhance coordination versatility, a tridentate NNP ligand was designed in which one nitrogen donor is replaced with a softer phosphorus atom. This modification is aimed at enhancing coordination versatility and enabling stabilization of metal in multiple oxidation states.

The NNP ligand was synthesized *via* a three-step procedure involving condensation of *N*-phenylethylenediamine with 2-(diphenylphosphino)benzaldehyde, reduction of the resulting imine with sodium borohydride, and subsequent condensation with pyridine-2-carboxaldehyde (Scheme 1). The ligand was isolated as a white solid and fully characterized by nuclear magnetic resonance (NMR) spectroscopy, electrospray ionization mass spectrometry (ESI-MS) (Fig. S1–S10), and single-crystal X-ray diffraction (SCXRD) (Fig. 1).

To investigate its coordination flexibility, we explored its interactions with a series of soft and hard metal centres, including Zn(II), Ni(II), Pd(II), Ru(II), Cu(I), and Cu(II). The reaction of NNP with anhydrous zinc(II) chloride led to the formation of a white precipitate (Fig. S11–S15). The SCXRD analysis reveals the structure of the complex as $[Zn(NNP)Cl_2]$, where the Zn(II) ion is present in a tetrahedral environment coordinated to nitrogen (N1) and phosphorus donor (P3) of the NNP ligand, along with two chloride atoms (Fig. 2).

Similarly, the reaction of NNP with anhydrous nickel(II) chloride in acetonitrile afforded a green coloured solid. The composition of the nickel complex was confirmed by ESI-MS and elemental analysis (Fig. S16–S18). The cyclic voltammogram of $[Ni(NNP)Cl_2]\cdot CH_3CN$ shows a reversible reduction event at −1.25 V (*vs.* Fc/Fc^+) for the Ni(II)/Ni(I) couple (Fig. S19). The SCXRD analysis confirmed the solid-state structure as $[Ni(NNP)Cl_2]\cdot CH_3CN$ (Fig. 2).

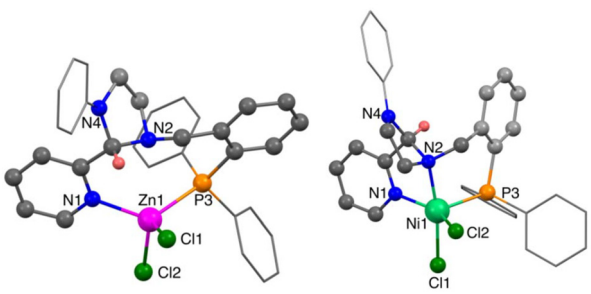

Fig. 2 Solid-state structure of $[Zn(NNP)Cl_2]$ (left) and $[Ni(NNP)Cl_2]\cdot CH_3CN$ (right). H atoms other than those bound to the stereogenic centre are omitted for clarity. Interatomic distances and angles are provided in the SI (Fig. S94 and S95, Tables S2 and S3).

Reaction of NNP with $[Pd(CH_3CN)_2Cl_2]$ afforded [Pd(NNP)Cl][Cl] confirmed by NMR spectroscopy, elemental analysis and ESI-MS (observed m/z = 640.0891, calcd 640.0901, Fig. S20–S25) and SCXRD, which shows Pd(II) in a square planar geometry (Fig. 3). Subsequent reaction with *p*-toluenethiol in the presence of triethylamine led to formation of $[Pd(NNP)(SPhCH_3)][Cl]$ (Fig. S26–S30), followed by anion exchange with KPF_6, yielded $[Pd(NNP)(SPhCH_3)][PF_6]$, characterized by NMR spectroscopy (Fig. S31 and S32) and SCXRD (Fig. 3).

Further, we investigated the reactivity of the NNP ligand with soft metal ions such as Ru(II). Reaction of NNP with $[Ru(PPh_3)_3Cl_2]$ afforded $[Ru(NNP)(PPh_3)Cl_2]$, characterized by NMR spectroscopy, ESI-MS, and elemental analysis (Fig. S33–S37). The crystal structure reveals an octahedral Ru(II) centre coordinated by the NNP ligand and a PPh_3 ligand (Fig. 4).

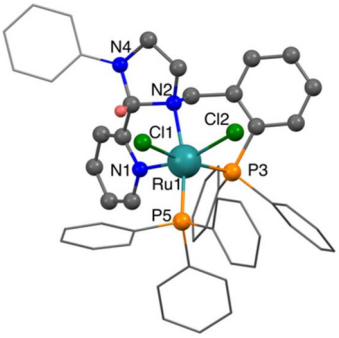

Fig. 4 Solid-state structure of $[Ru(NNP)(PPh_3)Cl_2]$. H atoms other than those bound to the stereogenic centre are omitted for clarity. Interatomic distances and angles are provided in the SI (Fig. S98 and Table S6).

Synthesis of ruthenium(II) borohydride complex and its reactivity

Phosphorus-containing ligands are known to stabilize ruthenium hydride species through their strong σ-donor and π-acceptor properties, which enhance electron density at the metal centre and improve overall stability.[57–60] Motivated by this, we sought to synthesize Ru(II) hydride complexes supported by an NNP ligand. Treatment of the NNP ligand with $[Ru(H)Cl(CO)(PPh_3)_3]$ in toluene at 118 °C under a nitrogen atmosphere afforded two distinct products, observed as a white precipitate and a yellow filtrate, which were further characterized by standard spectroscopy techniques (Fig. S38–S50). ^{1}H NMR analysis of the crude mixture indicated the presence of two stereoisomeric species (Fig. 5). Recrystallization of the precipitate yielded colourless crystals of *anti-rac*-[Ru(NNP)(H)Cl(CO)], while the filtrate provided *syn-rac*-[Ru(NNP)(H)Cl(CO)] (Fig. 6).

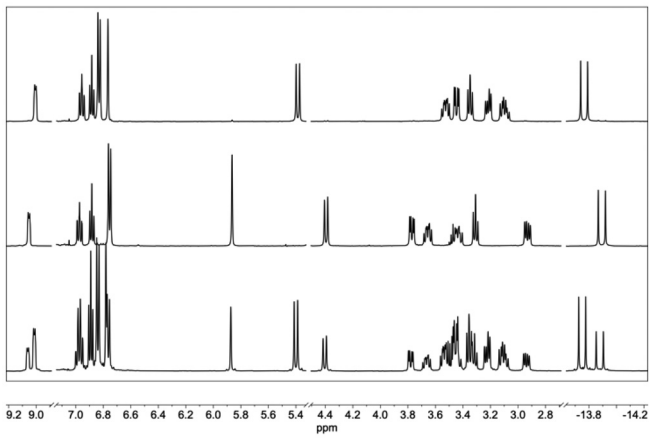

Fig. 5 ^{1}H NMR spectra of crude [Ru(NNP)(H)Cl(CO)] showing the presence of both *syn* and *anti*-complexes (bottom), isolated *syn-rac*-[Ru(NNP)(H)Cl(CO)] (middle), and *anti-rac*-[Ru(NNP)(H)Cl(CO)] (top).

The hydride transfer reactivity of both stereoisomers was evaluated with CS_2; however, no reactivity was observed (Fig. S51 and S52), likely due to the moderate *trans* influence of the chloride[61] positioned *trans* to the hydride. To further modulate the electronic, chloride substitution with borohydride was performed, affording the corresponding [Ru(NNP)(H)(η^1-BH_4)(CO)] isomers, which were characterized by NMR spectroscopy, and ESI-MS analysis (Fig. S53–S57).

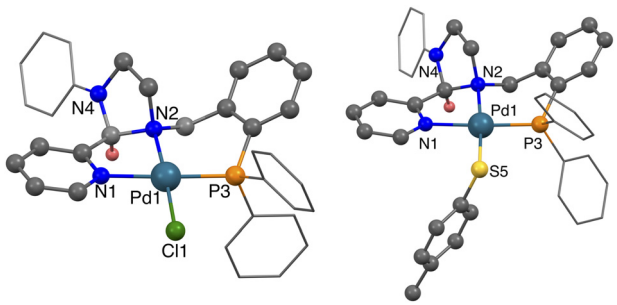

Fig. 3 Solid-state structures of [Pd(NNP)Cl][Cl] (left) and [Pd(NNP)(SPhCH$_3$)][PF$_6$] (right). H atoms other than those bound to the stereogenic centre and counter anion are omitted for clarity. Interatomic distances and angles are provided in the SI (Fig. S96 and S97, Tables S4 and S5).

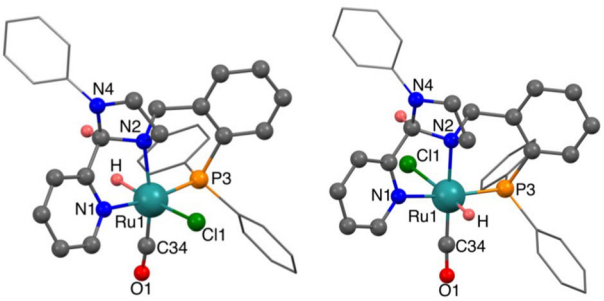

Fig. 6 Solid-state structure of *syn-rac*-[Ru(NNP)(H)Cl(CO)] (left) and *anti-rac*-[Ru(NNP)(H)Cl(CO)] (right). H atoms other than those bound to the stereogenic centre are omitted for clarity. Interatomic distances and angles are provided in the SI (Fig. S99 and S100, Tables S7 and S8).

The ^{1}H NMR spectrum of *anti-rac*-[Ru(NNP)(H)(η^1-BH_4)(CO)] (**1**) has characteristic peaks for ligand coordinated to ruthenium along with a broad peak at −1.56 ppm corresponding to the borohydride anion and a doublet peak at −11.83 ppm corresponding to Ru–H (Fig. S53). The SCXRD analysis confirmed the solid-state structure as *anti-rac*-[Ru(NNP)(H)(η^1-BH_4)(CO)], where Ru(II) is present in octahedral geometry, hydride ligand located *trans* to the η^1-coordinated borohydride ligand (Fig. 7) (Scheme 2).

Notably, the Ru–H bond length in (**1**) (1.55 Å) is elongated compared to that in [Ru(NNP)(H)Cl(CO)] (1.45 Å), indicating a weaker metal–hydride interaction. This elongation is consistent with enhanced hydride donor ability, attributed to increased electron density at the Ru centre provided by the borohydride ligand. The electron-rich environment is expected to facilitate insertion reactions with electrophilic substrates such as CS_2.The addition of carbon disulfide to a dichloromethane/ethanol (1 : 1) solution of complex (**1**) induced an immediate colour change from colourless to yellow, accompanied by precipitation of a yellow solid, which was fully characterized by NMR spectroscopy, ESI-MS and FTIR analysis (Fig. S58–S62). ^{1}H NMR spectroscopy revealed two singlets at 11.43 and 11.05 ppm, characteristic of the thioformate (–CS_2H) moiety, while signals corresponding to Ru–H and Ru–BH_4 were absent, consistent with hydride transfer and CS_2 insertion (Fig. S58). SCXRD confirmed the structure as [Ru(NNP)(CS_2H)$_2$(CO)] (**2**), in which the Ru(II) centre adopts an octahedral geometry with thioformate groups *trans* to each other (Fig. 7).

Subsequent treatment of (**2**) with excess methyl iodide (10 equivalents) in dichloromethane resulted in an immediate colour change from yellow to orange, indicating rapid transformation. This reaction generated free methyl dithioformate along with [Ru(NNP)I_2(CO)] (**3**), as confirmed by NMR spectroscopy (Fig. S63 and S64) and UV-vis analysis. The disappearance of the 350–400 nm absorption band of (**2**) and the emergence of a new band in the 400–450 nm region are consistent with the formation of (**3**), which was further supported by ESI-MS analysis (Fig. S65–S67).

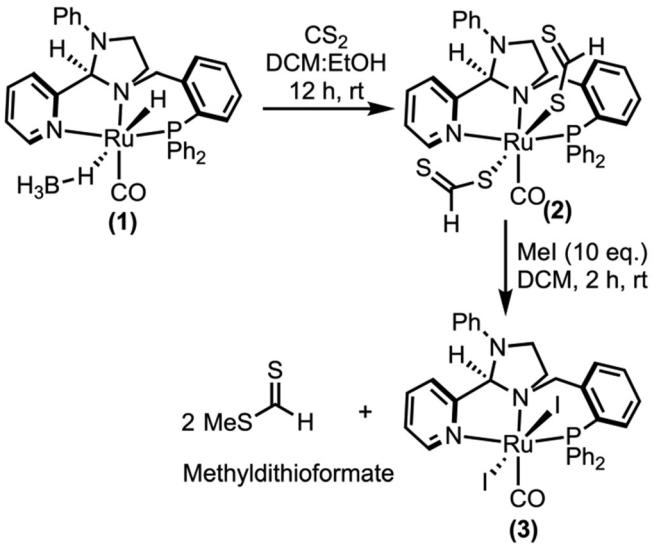

Scheme 2 Reactivity of Ruthenium borohydride complex.

Synthesis of copper(I) and copper(II) complexes

The coordination behaviour of the newly designed NNP ligand with copper was explored in both Cu(I) and Cu(II) oxidation states. Reaction of NNP with CuCl and CuI in acetonitrile afforded yellow crystalline complexes [Cu(NNP)Cl] and [Cu(NNP)I], respectively, which were characterized by NMR spectroscopy, ESI-MS, and SCXRD (Fig. S68–S73). In [Cu(NNP)I], the Cu–N and Cu–P bond lengths were 2.072(2), 2.160(3), and 2.180(8) Å, while the corresponding parameters in [Cu(NNP)Cl] were 2.076(2), 2.230(2), and 2.195(7) Å.

Cationic Cu(I) species were obtained by reacting NNP with [Cu(CH_3CN)$_4$][X] (X = PF_6, BF_4, OTf), affording [Cu(NNP)(CH_3CN)][X], confirmed by NMR and ESI-MS (Fig. S74–S79). Reaction with triphenylphosphine furnished [Cu(NNP)(PPh_3)][BF_4], characterized by NMR spectroscopy and SCXRD (Fig. S80 and S81). These results highlight the ability of the NNP framework to stabilize Cu(I) centres through its tridentate coordination environment (Fig. 8).

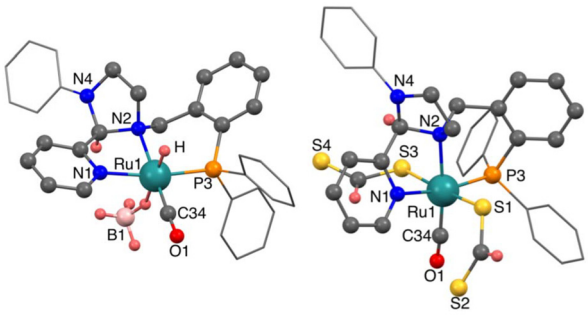

Fig. 7 Solid-state structure of *anti-rac*-[Ru(NNP)(H)(η^1-BH_4)(CO)] (left) and [Ru(NNP)(CS_2H)(CO)] (right). H atoms other than those bound to the stereogenic centre are omitted for clarity. Interatomic distances and angles are provided in the SI (Fig. S101 and S102, Tables S9 and S10).

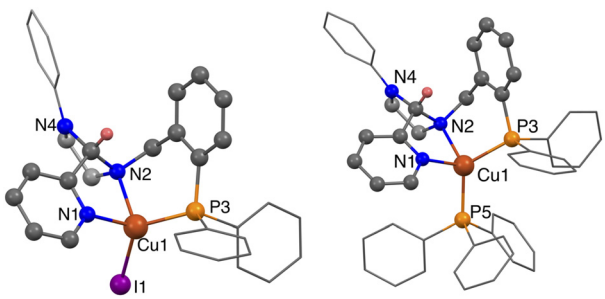

Fig. 8 Solid-state structure of [Cu(NNP)I] (left) and [Cu(NNP)(PPh_3)][BF_4] (right). H atoms other than those bound to the stereogenic centre are omitted for clarity. Interatomic distances and angles are provided in the SI (Fig. S103 and S104, Tables S11 and S12).

In contrast, reaction with Cu(II) chloride in dichloromethane afforded a green crystalline product, which was initially analysed by ESI-MS (Fig. S82 and S83). The SCXRD analysis confirmed the solid-state structure as $[Cu_2(NNP)_2(\mu\text{-}Cl)Cl_2][CuCl_2]$, in which Cu(II) adopts a square-pyramidal geometry (Fig. 9). The Cu-donor bond lengths (Cu–N(1) = 2.018(3) Å, Cu–N(2) = 2.087(4) Å, Cu–P(3) = 2.3216(12) Å) reveal a distinct donor preference: Cu(I) exhibits stronger coordination to the phosphorus donor, while Cu(II) shows enhanced affinity for nitrogen donors. This redox-dependent shift underscores the electronic adaptability of the NNP ligand in stabilizing both oxidation states.

Reduction of copper(II) to copper(I)

The reduction of $[Cu(NNP)Cl_2]$ was achieved using ascorbic acid as a mild and environmentally benign reductant. The UV-Vis spectrum of the Cu(II) precursor displayed a broad d–d transition in the 600–800 nm region, which gradually diminished upon incremental addition of ascorbic acid and disappeared completely, consistent with quantitative reduction to Cu(I) (Fig. S84). The formation of the diamagnetic Cu(I) product was further confirmed by NMR spectroscopy.

Transmetallation

A clean metal exchange was observed upon treatment of $[Zn(NNP)Cl_2]$ with CuI in acetonitrile, evidenced by an immediate colour change from colourless to yellow. ^1H and ^{31}P NMR titrations revealed the progressive disappearance of Zn(II)-bound resonances and the concomitant growth of new signals corresponding to [Cu(NNP)I], indicating complete displacement of Zn(II) under the experimental conditions (Fig. S85 and S86). The transformation was further validated by ESI-MS, which showed the $[(NNP)Cu]^+$ ion (observed m/z = 562.1477; calcd m/z = 562.1473, Fig. S87). These results demonstrate the high affinity of Cu(I) for the NNP framework and highlight the potential of this system to undergo controlled redox and metal-exchange processes.

Electrochemical studies of Cu(I) and Cu(II) complexes

The electrochemical behaviour of $[Cu(NNP)(CH_3CN)][OTf]$, $[Cu(NNP)(CH_3CN)][PF_6]$, [Cu(NNP)I], [Cu(NNP)Cl] and $[Cu(NNP)Cl_2]$ complexes was examined using cyclic voltammetry in acetonitrile with 0.1 M tetrabutylammonium hexafluorophosphate ($TBAPF_6$) as the supporting electrolyte. All complexes displayed a single, reversible Cu(II)/Cu(I) redox couple (Fig. S88–S92), indicative of a redox process centred on the copper ion.

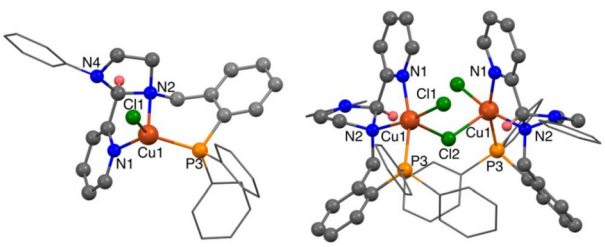

Fig. 9 Solid-state structure of [Cu(NNP)Cl] (left) and $[Cu_2(NNP)_2(\mu\text{-}Cl)Cl_2][CuCl_2]$ (right). H atoms other than those bound to the stereogenic centre are omitted for clarity. Interatomic distances and angles are provided in the SI (Fig. S105 and S106, Tables S13 and S14).

Biological activity screening

Antibacterial studies. Antimicrobial resistance (AMR) represents a major global health challenge and is projected to cause 10 million deaths annually by 2050.[62] Among the key contributors to AMR is *Staphylococcus aureus* (*S. aureus*), a pathogenic bacterium responsible for severe infections, including pneumonia, arthritis, and sepsis. *S. aureus* is capable of invading and proliferating within mammalian cells, particularly neutrophils and macrophages, leading to persistent and systemic infections. To assess the potential of the NNP scaffold and its metal derivatives, the free ligand and its complexes ($[Zn(NNP)Cl_2]$, [Pd(NNP)Cl][Cl], $[Ru(NNP)(PPh_3)Cl_3]$, *syn-rac*-[Ru(NNP)(H)Cl(CO)], *anti-rac*-[Ru(NNP)(H)Cl(CO)]), [Cu(NNP)I], $[Cu(NNP)(PPh_3)][BF_4]$, $[Cu(NNP)(CH_3CN)][BF_4]$, $[Cu(NNP)(CH_3CN)][OTf]$, $[Cu(NNP)(CH_3CN)][PF_6]$, [Cu(NNP)Cl] and $[Cu_2(NNP)_2(\mu\text{-}Cl)Cl_2][CuCl_2]$ were screened for antibacterial activity. The free ligand and metal precursors were inactive (MIC >64 μg mL^{-1}) (Table S15), whereas metalation substantially enhanced activity[63] (Table 1). The Pd(II) complex [Pd(NNP)Cl][Cl] displayed moderate activity (MIC 16 μg mL^{-1}) but limited selectivity (IC_{50} = 25.5 ± 3.5 μM against HEK-293). In contrast, the ruthenium complexes *syn-rac*-[Ru(NNP)(H)Cl(CO)] and *anti-rac*-[Ru(NNP)(H)Cl(CO)] exhibited superior potency (MIC 2 μg mL^{-1}). No effect of *syn* and *anti*-position of the hydride was observed in antimicrobial activity. Further, we calculated the selectivity index (SI) to evaluate the therapeutic window of antimicrobial agents by comparing their toxicity to mammalian cells with their antimicrobial efficacy. In our study, SI was calculated as the ratio of the 50% inhibitory concentration (IC_{50}) against the non-cancerous human embryonic kidney cell line (HEK-293) to the minimum inhibitory concentration (MIC) of the metal complexes against bacterial strains. A higher SI value indicates a greater degree of selectivity of the compound towards bacterial cells over mammalian cells, suggesting better therapeutic potential and reduced cytotoxicity.[64,65] The complex *anti-rac*-[Ru(NNP)(H)Cl(CO)] displayed a better selectivity index (~5) than *syn-rac*-[Ru(NNP)(H)Cl(CO)], signifying the relevance of the geometry in enhancing

Table 1 MIC (μg mL^{-1}) of NNP ligand and its metal complexes against *S. aureus* ATCC29213

Compound	*S. aureus* ATCC29213
NNP	>64
$[Zn(NNP)Cl_2]$	>64
[Pd(NNP)Cl][Cl]	16
$[Ru(NNP)(PPh_3)Cl_2]$	4
syn-rac-[Ru(NNP)(H)Cl(CO)]	2
anti-rac-[Ru(NNP)(H)Cl(CO)]	2
Levofloxacin	0.5

Table 2 Half-maximal inhibitory concentration (μM) of NNP ligand and its metal complexes against cancer cell lines

Compound	A549	MDA-MB-231	MCF-7	HEK-293
NNP	1.66 ± 0.68	1.86 ± 0.50	0.69 ± 0.20	2.30 ± 1.68
[Zn(NNP)Cl_2]	3.32 ± 0.30	1.81 ± 0.80	0.74 ± 0.30	41.67 ± 5.36
[Pd(NNP)Cl][Cl]	29.90 ± 4.12	5.55 ± 0.42	20.07 ± 0.08	25.50 ± 3.51
[Ru(NNP)(PPh_3)Cl_2]	16.52 ± 1.52	47.09 ± 2.12	21.01 ± 2.21	42.61 ± 4.78
syn-rac-[Ru(NNP)(H)Cl(CO)]	0.84 ± 0.17	1.16 ± 0.28	0.58 ± 0.30	0.92 ± 0.19
anti-rac-[Ru(NNP)(H)Cl(CO)]	0.51 ± 0.24	7.73 ± 2.85	3.70 ± 1.96	16.61 ± 2.67
Cisplatin	3.23 ± 0.20	4.07 ± 0.01	2.80 ± 0.42	1.21 ± 0.34

selectivity. Substitution of CO with PPh_3 slightly reduced potency (MIC 4 μg mL^{-1}) but significantly enhanced selectivity (IC_{50} = 42.6 ± 4.8 μM), underscoring the role of ancillary ligands in modulating biological activity. These findings highlight the potential of Ru–hydride carbonyl species as scaffolds for selective antibacterial agents.

The investigation into the effects of essential metals, specifically zinc and copper complexes, revealed that [Zn(NNP)Cl_2] exhibited no significant toxicity at concentrations exceeding 64 μg mL^{-1}, while copper complexes displayed moderate toxicity within the range of 8–16 μg mL^{-1} (Table S16). Notably, the most active compound, the ruthenium hydride complex, demonstrated a minimum inhibitory concentration (MIC) of 2 μg mL^{-1}, which is lower than that of the widely used antibiotic levofloxacin. Efforts to enhance structural modifications aimed at surpassing levofloxacin are currently in progress. The findings presented align closely with the data from the Community for Open Antimicrobial Drug Discovery (CO-ADD) study, which identified ruthenium as the most frequently detected element in active 'non-toxic' compounds.[66] This observation underscores the potential of Ru–hydride carbonyl species as effective scaffolds for the development of selective antibacterial agents.

Cytotoxicity against cancer cell lines. The cytotoxicity of the ligand and its complexes was further evaluated against three cancer cell lines (Human lung adenocarcinoma cell line A549, Breast adenocarcinoma cell lines MDA-MB-231, and MCF-7) and one non-cancerous Human embryonic kidney cell line (HEK-293) using *in vitro* assays. The IC_{50} values are summarized in Table 2.

Among the series, *anti-rac*-[Ru(NNP)(H)Cl(CO)] displayed the most potent and selective activity (IC_{50} = 0.51 ± 0.24 μM in A549; IC_{50} = 16.6 ± 2.7 μM in HEK-293), suggesting a favourable therapeutic window. The *syn*-isomer, though equally potent (IC_{50} ≈ 0.9 μM), was broadly cytotoxic, including towards non-cancerous cells, limiting its selectivity.

Interestingly, [Zn(NNP)Cl_2] exhibited strong and selective cytotoxicity across cancer lines (IC_{50} = 0.7–3.3 μM) while showing negligible toxicity in HEK-293 (IC_{50} ≈ 41.7 μM). This marked difference suggests that coordination with zinc may enhance selective cytotoxicity, potentially due to altered uptake or cellular interactions.[67] The Pd(II) derivative displayed moderate activity in MDA-MB-231 cells but lacked selectivity, whereas [Ru(NNP)(PPh_3)Cl_2] was generally less active (IC_{50} = 16–47 μM). Cisplatin, used as a control, exhibited potent but non-selective cytotoxicity (IC_{50} = 1.2 μM in HEK-293), highlighting the advantage of the NNP metal complexes in balancing potency and reduced off-target effects. In general, $ZnCl_2$ is regarded as non-toxic to cancer cells under typical experimental conditions.[68] Palladium chloride analogues are known to undergo ultra-fast hydrolysis in biological media, which limits Pd(II) ions from effectively interacting with cellular targets, suggesting low intrinsic toxicity of these Pd(II) precursors.[69] However, when properly coordinated with tailored ligands, palladium complexes often show enhanced cytotoxicity. Also, ruthenium precursor complex [RuHCl(CO)(PPh_3)$_3$] has been reported to exhibit negligible cytotoxicity even at concentrations as high as 100 μM.[70] These findings imply that the moderate cytotoxicity observed in our metal complexes likely arises from the precise tuning of the ligand environment around the metal center rather than from the metal salts themselves. This ligand modulation plays a crucial role in dictating biological activity and selectivity. In particular, *syn*,*anti*-[Ru(NNP)(H)Cl(CO)] and [Zn(NNP)Cl_2] complexes stand out as dual-action candidates, combining potent antibacterial and anticancer activity with improved selectivity relative to established metallodrugs.

Conclusions

In summary, a novel koneramine-derived tridentate NNP ligand has been developed that stabilizes a broad range of metal centres through its mixed-donor environment. The ligand displays notable electronic flexibility, supporting both low and high valent species of Cu, Ru, Zn, Pd and Ni. The ruthenium borohydride complexes exhibit distinct reactivity, including hydride transfer and CS_2 insertion into the Ru–H bond. Biological studies revealed potent antibacterial and anticancer activities, with *syn-rac*-[Ru(NNP)(H)Cl(CO)] and *anti-rac*-[Ru(NNP)(H)Cl(CO)] showing MIC values of 2 μg mL^{-1} against *S. aureus*. Furthermore, *anti-rac*-[Ru(NNP)(H)Cl(CO)] and [Zn(NNP)Cl_2] show enhanced potency and lower toxicity toward non-cancerous cells when compared to cisplatin. These results establish the NNP scaffold as a versatile platform for both coordination chemistry and metallodrug development.

Author contributions

A. Y. performed the synthesis and analysis. A. Y. and R. J. B. refined the crystal data. S. D., K. C. and R. G. performed biological activity experiments. A. Y. and R. A. wrote the manuscript.

Conflicts of interest

The authors declare no conflicts of interest.

Data availability

The data supporting this article have been included as part of the supplementary information (SI). Supplementary information: original images and data, synthetic procedures and experimental details. See DOI: https://doi.org/10.1039/d5dt02106e.

CCDC 2472269–2472273, 2472461–2472468 and 2472560 contain the supplementary crystallographic data for this paper.[71a–n]

Acknowledgements

The financial support for this work was from the ANRF, India (CRG/2020/001708). A. Y. is a recipient of the Prime Minister's Research Fellowship. S. D. and K. C. acknowledge the Ministry of Education, India, for their fellowship.

References

1 M. Sirignano, A. Mariconda, G. Vigliotta, J. Ceramella, D. Iacopetta, M. S. Sinicropi and P. Longo, *Catalysts*, 2022, **12**, 18.
2 G. Venkatachalam and R. Ramesh, *Spectrochim. Acta, Part A*, 2005, **61**, 2081–2087.
3 P. Tharmaraj, D. Kodimunthiri, P. Prakash and C. D. Sheela, *J. Coord. Chem.*, 2009, **62**, 2883–2892.
4 M. S. S. Adam, M. M. Makhlouf, A. Alharbi and N. M. El-Metwaly, *J. Mol. Liq.*, 2022, **351**, 118620.
5 H. Madec, F. Figueiredo, K. Cariou, S. Roland, M. Sollogoub and G. Gasser, *Chem. Sci.*, 2023, **14**, 409–442.
6 L. Piccirilli, D. Lobo Justo Pinheiro and M. Nielsen, *Catalysts*, 2020, **10**, 773.
7 S. Raje, S. Gurusamy, A. Koner, S. Mehrotra, S. J. Jennifer, P. G. Vasudev, R. J. Butcher and R. Angamuthu, *Chem. – Asian J.*, 2016, **11**, 128–135.
8 S. Raje, K. Mani, M. MinnathParsutkar and R. Angamuthu, *New J. Chem.*, 2017, **41**, 12303–12308.
9 S. Raje, N. Mondivagu, M. Chahal, R. J. Butcher and R. Angamuthu, *Chem. – Asian J.*, 2018, **13**, 1458–1466.
10 M. Chahal, S. Raje, G. Kotana and R. Angamuthu, *Green Chem.*, 2019, **21**, 6372–6380.
11 S. Ghosh, A. Akhir, D. Saxena, S. Singh, S. Sivakumar, S. Chopra and R. Angamuthu, *Dalton Trans.*, 2022, **51**, 15659–15668.
12 S. Raje, A. Koner, S. Ghosh, R. J. Butcher, L. Mathivathanan, M. Sundararajan and R. Angamuthu, *Chem. – Asian J.*, 2023, **18**, e202300706.
13 F.-B. Han, Y.-L. Zhang, X.-L. Sun, B.-G. Li, Y.-H. Guo and Y. Tang, *Organometallics*, 2008, **27**, 1924–1928.
14 G. Tan and H. Zhu, *Inorg. Chem.*, 2011, **50**, 6979–6986.
15 C. Holzhacker, M. J. Calhorda, A. Gil, M. D. Carvalho, L. P. Ferreira, K. Mereiter, B. Stöger, E. Pittenauer, G. Allmaier and K. Kirchner, *Polyhedron*, 2014, **81**, 45–55.
16 R. Zhuang, H. Liu, J. Guo, B. Dong, W. Zhao, Y. Hu and X. Zhang, *Eur. Polym. J.*, 2017, **93**, 358–367.
17 N. Kurisu, E. Asano, Y. Hatayama, Y. Kurihara, T. Hashimoto, K. Funatsu, K. Ueda and Y. Yamaguchi, *Eur. J. Inorg. Chem.*, 2019, **2019**, 126–133.
18 X. Feng, J. Li and Z. Yang, *Catalysts*, 2022, **12**, 760.
19 L. Zhang, Q. Chen, L. Li, J. Jiang, H. Sun, L. Li, T. Liu, L. Zhang and C. Li, *RSC Adv.*, 2022, **12**, 14912–14916.
20 V. Papa, J. Fessler, F. Zaccaria, J. Hervochon, P. Dam, C. Kubis, A. Spannenberg, Z. Wei, H. Jiao, C. Zuccaccia, A. Macchioni, K. Junge and M. Beller, *Chem. – Eur. J.*, 2023, **29**, e202202774.
21 P. Song, H. Rong, T. Meng, Z. Cui, M. Mao and C. Yang, *Org. Biomol. Chem.*, 2024, **22**, 5112–5116.
22 H. Wang, J.-K. Liu, Y.-D. Wang, X.-Q. Hao, M.-P. Song, J.-F. Gong and H. Jiang, *Molecules*, 2025, **30**, 1530.
23 D. Majumdar, A. Bhanarkar, C. Rao and D. Gouda, *Atmos. Environ.:X*, 2022, **13**, 100157.
24 Y. Yan, C. Wang, Z. Zheng, L. Qu, D. Zeng and M. Li, *BMC Nephrol.*, 2019, **20**, 377.
25 M. Pappuswamy, A. Chaudhary, A. Meyyazhagan, K. K. Alagamuthu, B. Balasubramanian, V. A. Arumugam and J. K. Sebastian, *Asian Pac. J. Cancer Prev.*, 2023, **24**, 357–361.
26 F. Gholami, S. Ansari, B. Larijani and M. Mahdavi, *J. Organomet. Chem.*, 2023, **992**, 122663.
27 M. Wang and X. Jiang, *ACS Sustainable Chem. Eng.*, 2022, **10**, 671–677.
28 L. Wang, H. Sun, Z. Zuo, X. Li, W. Xu, R. Langer, O. Fuhr and D. Fenske, *Eur. J. Inorg. Chem.*, 2016, **2016**, 5205–5214.
29 L. D. Field, E. T. Lawrenz, W. J. Shaw and P. Turner, *Inorg. Chem.*, 2000, **39**, 5632–5638.
30 X. Shi, T. Rajeshkumar, L. Maron and J. Cheng, *Chem. Commun.*, 2022, **58**, 1362–1365.
31 L. D. Field, P. M. Jurd, A. M. Magill and M. M. Bhadbhade, *Organometallics*, 2013, **32**, 636–642.
32 C. Z. Ye, I. Del Rosal, E. T. Ouellette, S. Hohloch, L. Maron, C. Camp and J. Arnold, *Chem. Commun.*, 2024, **60**, 12377–12380.
33 A. S. Tossaint, C. Rebreyend, V. Sinha, M. Weber, S. Canossa, E. A. Pidko and G. A. Filonenko, *Catal. Sci. Technol.*, 2022, **12**, 2972–2977.
34 J. Paik, J. H. Choe, S. Padmanaban, M. Seo, C.-J. Yoo, H. B. Lee and Y. Lee, *JACS Au*, 2025, **5**, 811–821.
35 X. Feng, J. Li and Z. Yang, *Catalysts*, 2022, **12**, 760.
36 S. Chakraborty, J. Zhang, Y. J. Patel, J. A. Krause and H. Guan, *Inorg. Chem.*, 2013, **52**, 37–47.
37 C. M. Zall, J. C. Linehan and A. M. Appel, *J. Am. Chem. Soc.*, 2016, **138**, 9968–9977.
38 M. Barakat, S. Elhajj, R. Yazji, A. J. M. Miller and F. Hasanayn, *Inorg. Chem.*, 2024, **63**, 12133–12145.

39 F. Schneck, J. Ahrens, M. Finger, A. C. Stückl, C. Würtele, D. Schwarzer and S. Schneider, *Nat. Commun.*, 2018, **9**, 1161.
40 M. Zhang, X. Liang, Y. Wang, H. Yang and G. Liang, *Catalysts*, 2022, **12**, 790.
41 M. A. Fischbach and C. T. Walsh, *Science*, 2009, **325**, 1089–1093.
42 K. Mani, D. Deng, C. Lin, M. Wang, M. L. Hsu and N. G. Zaorsky, *Nat. Commun.*, 2024, **15**, 1519.
43 S. K. Nandanwar and H. J. Kim, *ChemistrySelect*, 2019, **4**, 1706–1721.
44 S. Ray, R. Mohan, J. K. Singh, M. K. Samantaray, M. M. Shaikh, D. Panda and P. Ghosh, *J. Am. Chem. Soc.*, 2007, **129**, 15042–15053.
45 W. Sun, Y. Jian, M. Zhou, Y. Yao, N. Tian, C. Li, J. Chen, X. Wang and Q. Zhou, *J. Med. Chem.*, 2021, **64**, 7359–7370.
46 J. Wang, Y. Song, Z. Huang, W. Lin, G. Yu, Y. Xiong, G. Jiang, Y. Tan, J. Wang and X. Liao, *J. Med. Chem.*, 2023, **66**, 13304–13318.
47 H. F. Abd El-Halim, G. G. Mohamed and M. N. Anwar, *Appl. Organomet. Chem.*, 2017, **32**, e3899.
48 H. F. Abd El-Halim, M. M. Omar and M. N. Anwar, *J. Therm. Anal. Calorim.*, 2017, **130**, 1069–1083.
49 R. Mondal, M. Keerthana, N. Pandurangan and S. Shanmugaraju, *ChemMedChem*, 2024, **19**, e202400558.
50 A. Climova, E. Pivovarova, M. Szczesio, K. Gobis, D. Ziembicka, A. Korga-Plewko, J. Kubik, M. Iwan, M. Antos-Bielska, M. Krzyzowska and A. Czylkowska, *J. Inorg. Biochem.*, 2023, **240**, 112108.
51 S. Sen, N. Chowdhury, T. W. Kim, M. Paul, D. Debnath, S. Jeon, A. Bagchi, J. Im and G. Biswas, *Bioinorg. Chem. Appl.*, 2022, **2022**, 8453159.
52 D. Bhosale, A. Chopade, S. Nimal, R. Gacche, D. Raut, P. Chaudhari, G. Puri, R. Khobragade, A. Narale, M. Hublikar, P. Pisal and A. Lawand, *Appl. Organomet. Chem.*, 2024, **39**, e7904.
53 K. Chaudhary, B. Agrahari, B. Biswas, N. Chatterjee, A. Chaudhary, A. Kumar, H. Sonker, S. Dewan, D. Saxena, A. Akhir, N. Malhotra, S. Chopra, S. Misra, S. Matheswaran and R. G. Singh, *Adv. Healthcare Mater.*, 2024, **13**, e2400378.
54 B. Agrahari, K. Chaudhary, S. Dewan, H. Sonker, V. A. S. A. Chandra, N. Awasthi, H. Makari, S. Sinharay and R. G. Singh, *Small*, 2025, e2503986.
55 E. T. Adman, *Adv. Protein Chem.*, 1991, **42**, 145–197.
56 D.-H. Lee, L. Q. Hatcher, M. A. Vance, R. Sarangi, A. E. Milligan, A. A. Narducci Sarjeant, C. D. Incarvito, A. L. Rheingold, K. O. Hodgson, B. Hedman, E. I. Solomon and K. D. Karlin, *Inorg. Chem.*, 2007, **46**, 6056–6068.
57 J. Zhang, M. Gandelman, L. J. W. Shimon, H. Rozenberg and D. Milstein, *Organometallics*, 2004, **23**, 4026–4033.
58 H. Salem, L. J. W. Shimon, Y. Diskin-Posner, G. Leitus, Y. Ben-David and D. Milstein, *Organometallics*, 2009, **28**, 4791–4806.
59 C. Gunanathan and D. Milstein, *Chem. Rev.*, 2014, **114**, 12024–12087.
60 A. Phanopoulos, N. J. Brown, A. J. P. White, N. J. Long and P. W. Miller, *Inorg. Chem.*, 2014, **53**, 3742–3752.
61 T. Liu, Z. Liu, L. Tang, J. Li and Z. Yang, *Catalysts*, 2021, **11**, 1356.
62 L. J. Shallcross, S. J. Howard, T. Fowler and S. C. Davies, *Philos. Trans. R. Soc., B*, 2015, **370**, 20140082.
63 A. Frei, A. D. Verderosa, A. G. Elliott, J. Zuegg and M. A. T. Blaskovich, *Nat. Rev. Chem.*, 2023, **7**, 202–224.
64 Y. Lyu, Y. Yang, X. Lyu, N. Dong and A. Shan, *Sci. Rep.*, 2016, **6**, 27258.
65 S. Sosiangdi, L. Taemaitree, A. Tankrathok, S. Daduang, S. Boonlue, S. Klaynongsruang and N. Jangpromma, *Sci. Rep.*, 2023, **13**, 16096.
66 A. Frei, J. Zuegg, A. G. Elliott, M. Baker, S. Braese, C. Brown, F. Chen, G. D. C. G. Dujardin, N. Jung, A. P. King, A. M. Mansour, M. Massi, J. Moat, H. A. Mohamed, A. K. Renfrew, P. J. Rutledge, P. J. Sadler, M. H. Todd, C. E. Willans, J. J. Wilson, M. A. Cooper and M. A. T. Blaskovich, *Chem. Sci.*, 2020, **11**, 2627–2639.
67 F.-Y. Wang, Q.-Y. Xi, K.-B. Huang, X.-M. Tang, Z.-F. Chen, Y.-C. Liu and H. Liang, *J. Inorg. Biochem.*, 2017, **169**, 23–31.
68 M. Porchia, M. Pellei, F. Del Bello and C. Santini, *Molecules*, 2020, **25**, 5814.
69 A. Kazimir, B. Schwarze, P. Lönnecke, S. Jelača, S. Mijatović, D. Maksimović-Ivanić and E. Hey-Hawkins, *Pharmaceutics*, 2023, **15**, 682.
70 T. S. Kamatchi, P. Kalaivani, F. R. Fronczek, K. Natarajan and R. Prabhakaran, *RSC Adv.*, 2016, **6**, 46531–46547.
71 (*a*) CCDC 2472269: Experimental Crystal Structure Determination, 2025, DOI: 10.5517/ccdc.csd.cc2nzlmw; (*b*) CCDC 2472270: Experimental Crystal Structure Determination, 2025, DOI: 10.5517/ccdc.csd.cc2nzlnx; (*c*) CCDC 2472271: Experimental Crystal Structure Determination, 2025, DOI: 10.5517/ccdc.csd.cc2nzlpy; (*d*) CCDC 2472272: Experimental Crystal Structure Determination, 2025, DOI: 10.5517/ccdc.csd.cc2nzlqz; (*e*) CCDC 2472273: Experimental Crystal Structure Determination, 2025, DOI: 10.5517/ccdc.csd.cc2nzlr0; (*f*) CCDC 2472461: Experimental Crystal Structure Determination, 2025, DOI: 10.5517/ccdc.csd.cc2nzst8; (*g*) CCDC 2472462: Experimental Crystal Structure Determination, 2025, DOI: 10.5517/ccdc.csd.cc2nzsv9; (*h*) CCDC 2472463: Experimental Crystal Structure Determination, 2025, DOI: 10.5517/ccdc.csd.cc2nzswb; (*i*) CCDC 2472464: Experimental Crystal Structure Determination, 2025, DOI: 10.5517/ccdc.csd.cc2nzsxc; (*j*) CCDC 2472465: Experimental Crystal Structure Determination, 2025, DOI: 10.5517/ccdc.csd.cc2nzsyd; (*k*) CCDC 2472466: Experimental Crystal Structure Determination, 2025, DOI: 10.5517/ccdc.csd.cc2nzszf; (*l*) CCDC 2472467: Experimental Crystal Structure Determination, 2025, DOI: 10.5517/ccdc.csd.cc2nzt0h; (*m*) CCDC 2472468: Experimental Crystal Structure Determination, 2025, DOI: 10.5517/ccdc.csd.cc2nzt1j; (*n*) CCDC 2472560: Experimental Crystal Structure Determination, 2025, DOI: 10.5517/ccdc.csd.cc2nzx0l.